European Polymer Journal 255 (2026) 114877

Contents lists available at ScienceDirect

European Polymer Journal

journal homepage: www.elsevier.com/locate/europolj

Bio-derived isosorbide–siloxane molecular hybrid epoxy resins for fast-curing and degradable high-performance adhesives

Gwang-Mun Choi *, Jin-Hyuk Oh, Ki-Seok Jang, Yong-Sung Eom, Kwang-Seong Choi

Artificial Intelligence Creative Research Laboratory, Creative & Basic Technology Research Division, Low-Carbon Integration Technology Creative Research Section, Electronics and Telecommunications Research Institute (ETRI), 218 Gajeong-ro, Yuseong-gu, Daejeon 34129, Republic of Korea

ARTICLE INFO

Keywords:
Bio-based epoxy
Molecular hybrid materials
Siloxane network
Sustainable thermoset
High-performance adhesive

ABSTRACT

Cycloaliphatic epoxy resins are widely used in electronic and structural adhesive applications because of their excellent thermal stability and mechanical performance. However, conventional epoxy systems often require inorganic fillers to achieve sufficient thermomechanical performance and generally lack inherent degradability, thus raising concerns regarding end-of-life management. Here, we report an epoxy-functionalized isosorbide–siloxane molecular hybrid resin (EIS) synthesized via base-catalysed condensation of bio-derived isosorbide and an epoxy-functional alkoxysilane. The resulting oligomer preserves cycloaliphatic epoxide groups for subsequent cationic curing while incorporating hydrolytically labile silyl ether linkages within the backbone. Compared with the reference cycloaliphatic epoxy formulation, the EIS-based resin exhibits accelerated cationic curing behaviour and forms a cured hybrid network with improved thermomechanical performance and die-attach adhesion. In addition, the incorporation of alkali-labile Si–O–C silyl ether linkages enables alkaline-triggered degradation, providing a chemically addressable pathway for end-of-life disassembly. These results demonstrate that molecular-level integration of rigid bio-derived segments with an inorganic siloxane framework provides filler-free reinforcement while introducing a chemically addressable degradation pathway. This molecular hybrid design is a promising strategy for developing fast-curing, high-performance, degradable epoxy adhesives for sustainable electronic and structural applications.

1. Introduction

Epoxy thermosets, particularly cycloaliphatic epoxy systems, are widely used in electronic packaging, optical materials, structural adhesives, and composite matrices because of their excellent thermal stability, mechanical strength, and efficient cationic curing behaviour [1–6]. However, conventional epoxy networks generally rely on inorganic fillers to achieve high thermomechanical performance in demanding applications, which can lead to filler aggregation, interfacial incompatibility, and stress concentration at filler–matrix interfaces [7,8]. In addition, their highly crosslinked carbon-based network structures make degradation and end-of-life recycling difficult. Developing epoxy systems that combine high performance, rapid processing, and controlled degradability therefore remains an important challenge.

Bio-derived monomers provide a promising route to more sustainable high-performance polymer networks. Among them, isosorbide is an attractive rigid bicyclic diol derived from glucose and has been shown to enhance glass transition temperature and mechanical properties when incorporated into polymer backbones [9–13]. Nevertheless, the molecular-level integration of bio-derived isosorbide with inorganic siloxane structures in epoxy thermosets remains relatively unexplored.

In this work, we report an epoxy-functionalized isosorbide-siloxane molecular hybrid resin (EIS) synthesized through base-catalysed co-condensation of isosorbide and an epoxy-functional alkoxysilane, followed by cationic thermal curing. This molecular hybridization strategy covalently integrates rigid bio-derived organic segments and an inorganic siloxane framework within a single epoxy oligomer, eliminating the need for extrinsic inorganic fillers. The resulting hybrid resin preserves cycloaliphatic epoxide functionalities for rapid cationic curing while incorporating hydrolytically labile silyl ether linkages as chemically addressable degradation sites. By combining fast curing, high thermomechanical and adhesive performance, and controlled alkaline degradability, this work establishes a molecular design strategy for sustainable high-performance epoxy adhesives for electronic packaging and related structural applications.

* Corresponding author.
E-mail address: gmchoi@etri.re.kr (G.-M. Choi).

https://doi.org/10.1016/j.eurpolymj.2026.114877
Received 24 March 2026; Received in revised form 29 May 2026; Accepted 2 June 2026
Available online 4 June 2026

2. Materials and Methods

2.1. Materials

2-(3,4-Epoxycyclohexyl)ethyltrimethoxysilane (ECTMS, ≥99.9%) was purchased from ShinEtsu (Japan). Bio-derived isosorbide (≥99.9%) was supplied by Samyang (Daejeon, Korea). Barium hydroxide monohydrate ($Ba(OH)_2{\cdot}H_2O$, ≥98.0%) was purchased from Merck (Darmstadt, Germany) and used as the base catalyst for the co-condensation reaction. Tetraethylammonium bromide (TEAB, ≥99%), acetic anhydride (≥99.5%), anhydrous dichloromethane (≥99.8%), Crystal Violet, and glacial acetic acid were purchased from Merck (Darmstadt, Germany). Perchloric acid ($HClO_4$) solution in glacial acetic acid (0.1 N) was purchased from Thermo Fisher Scientific (Waltham, MA, USA). These reagents were used as received for epoxy equivalent weight (EEW) titration. TAG-2678 was obtained from King Industries (Norwalk, Connecticut, USA) and used as a thermal acid generator (TAG) for cationic polymerization of epoxides. Chloroform-d ($CDCl_3$, 99.8 atom % D) containing 0.1% (v/v) of tetramethylsilane (TMS) was purchased from Merck (Darmstadt, Germany) and used as the solvent and the internal standard for liquid-state nuclear magnetic resonance (NMR) analysis. Tetrahydrofuran (THF, ≥99.9%) stabilized with butylated hydroxytoluene was obtained from Samchun Chemicals (Pyeongtaek, Korea) and used as the mobile phase for gel permeation chromatography (GPC). PolyCAL™ PS105K and PolyCAL™ PS240K were purchased from Malvern Panalytical (Malvern, UK) and used as polystyrene standards for the GPC analysis. Bis(7-oxabicyclo[4.1.0]heptan-3-ylmethyl) adipate (CE, ≥90.0%) was purchased from Tokyo Chemical Industry (Japan) and evaluated as the reference cycloaliphatic epoxy resin for comparative studies. Phosphate-buffered saline (PBS) and 1 M sodium hydroxide aqueous solution (NaOH(aq)) were purchased from Merck (Darmstadt, Germany). Glacial acetic acid was diluted to prepare a 50 wt% aqueous acetic acid solution (AcOH(aq)), which was used as the acidic environment for degradation tests. Sodium chloride (NaCl, ≥99.5%) was purchased from Merck (Darmstadt, Germany) and used to prepare a saturated NaCl aqueous solution for the accelerated humid-aging test. All chemicals were used as received without any further purification.

2.2. Synthesis of EIS

EIS was synthesized via base-catalysed co-condensation of ECTMS with isosorbide, as illustrated in Fig. 1. In a typical synthesis, ECTMS (48.000 g, 195 mmol), isosorbide (42.707 g, 292 mmol), $Ba(OH)_2{\cdot}H_2O$ (0.092 g, 0.486 mmol, corresponding to 0.972 mmol OH equivalents), and deionized water (0.018 g, 1.0 mmol) were placed into a 250 mL flask equipped with a mechanical stirring and nitrogen purging system. The mixture was first stirred at 100 °C for 4 h under a closed nitrogen atmosphere to promote hydrolysis and initial condensation. The reaction was then continued at 100 °C for an additional 26 h under continuous nitrogen purging in a system open to the nitrogen outlet, allowing volatile condensation byproducts, primarily methanol, to be removed during the reaction.

After the reaction, residual volatile byproducts were further removed under vacuum at 60 °C for 1 h. The resulting EIS was obtained as a slightly yellowish, transparent resin. The resin recoveries after volatile removal were 85.6%, 86.1%, and 85.4% for three independently prepared batches, denoted as EIS-B1, EIS-B2, and EIS-B3, respectively.

2.3. Characterization of molecular structure of EIS

The molecular structure of EIS was studied using Fourier transform infrared (FTIR) spectroscopy, GPC, and liquid-state ^1H, ^{13}C, and ^{29}Si NMR spectroscopy. The FTIR spectra of EIS, isosorbide, and ECTMS were recorded using a Nicolet iS50 analytical FTIR spectrometer equipped with a built-in diamond ATR accessory (Thermo Fisher Scientific, Waltham, Massachusetts, USA). The GPC analysis of EIS was carried out at 35 °C using an OMNISEC GPC/SEC system equipped with four Viscotek T-columns (T-4000, T-3000, T-2000, T-1000) and triple detectors consisting of a differential refractive index detector, a light scattering detector, and a viscometer (Malvern Panalytical, Malvern, UK). THF was used as the mobile phase and PolyCAL™ PS105K, which has a weight-average molecular weight (M_w) of 103,136 g mol^{-1}, was used as a narrow standard material to calibrate the triple detectors. To verify the calibration of the GPC triple detector system, PolyCAL™ PS240K (M_w is 237,180 g mol^{-1}) was used as the reference material. The measured M_w value was within ± 2% of the certified value, as shown in Table S1, and thus confirmed an appropriate detector response and system alignment. Using the same triple-detection GPC system, absolute molecular weight parameters, including number-average molecular weight (M_n), and M_w, as well as hydrodynamic properties such as intrinsic viscosity (η) and hydrodynamic radius (Rh), were simultaneously determined. The liquid-state ^1H, ^{13}C, and ^{29}Si NMR spectra of EIS were recorded on a Bruker Avance III 400 spectrometer with $CDCl_3$ containing 0.1% (v/v) TMS as the solvent and internal standard. The NMR spectra were analysed using Mnova NMR software.

2.4. Formulation and thermal reaction analyses of EIS- and CE-Based curable resins

Thermal curing of EIS and CE was achieved via cationic ring-opening polymerization of their epoxide groups using TAG-2678. The EEWs of EIS and CE were measured in triplicate using a TEAB–$HClO_4$ titration method [14]. The resins were titrated in a non-aqueous dichloromethane/TEAB/acetic anhydride medium with commercially standardized 0.1 N $HClO_4$ in glacial acetic acid using Crystal Violet as the indicator. A reagent blank was measured in parallel, and the EEW values were calculated from the blank-corrected titrant volume. The measured EEW values were 401 ± 12 g eq^{-1} for EIS and 204 ± 7 g eq^{-1} for CE. Based on these EEW values, the EIS-based curable resin (r-EIS) was prepared by mixing EIS and TAG-2678 at a weight ratio of 100:0.5 using a paste mixer. The CE-based curable resin (r-CE) was prepared by mixing CE and TAG-2678 at a weight ratio of 100:1 using the same paste mixer. These formulations correspond to comparable epoxy-equivalent-normalized catalyst loadings of approximately 2.0 g TAG per epoxy equivalent for both r-EIS and r-CE (Table S2). Thus, the different resin-mass-based TAG loadings were selected to provide comparable catalyst

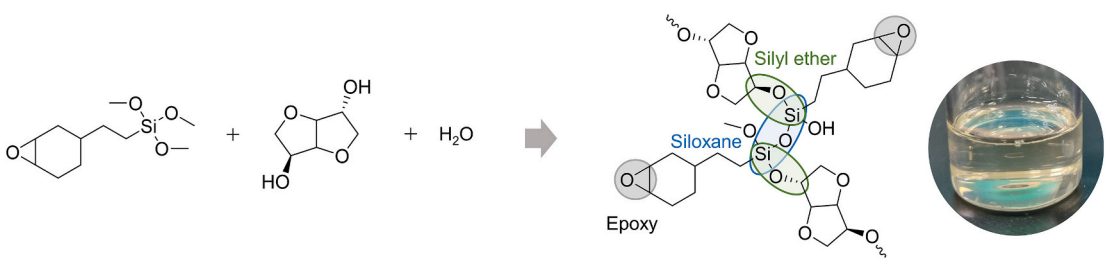

Fig. 1. Schematic illustration of the molecular design and formation of EIS via co-condensation of isosorbide and ECTMS, generating Si–O–Si siloxane and Si–O–C silyl ether linkages while preserving epoxide functionality.

amounts relative to the epoxy equivalents of each resin. The curing kinetics of r-EIS and r-CE were investigated by differential scanning calorimetry (DSC) under a nitrogen atmosphere using a DSC 204 F1 *Phoenix*® equipped with an IC 85 cooling system (Netzsch, Selb, Germany). Dynamic scans were performed at 10 °C min^{-1}, and isothermal measurements were conducted at 110, 115, and 120 °C. DSC kinetic analysis was performed using three independent measurement sets for each resin formulation. Each set included one dynamic DSC measurement and isothermal DSC measurements at the three temperatures described above. The dynamic DSC parameters, including the exothermic peak temperature (T_{peak}) and total reaction enthalpy (ΔH_{total}), were extracted from the dynamic scans, while the isothermal conversion profiles were fitted using the modified autocatalytic model. Arrhenius analysis was then performed for each independent measurement set based on the fitted rate constants.

2.5. Characterization of cured networks from r-EIS and r-CE

Based on the isothermal DSC results, r-EIS and r-CE were thermally cured at 120 °C for 10 min and 100 min, respectively. The resulting cured networks are denoted as c-EIS and c-CE, respectively. The thermomechanical properties of c-EIS and c-CE were evaluated by thermogravimetric analysis (TGA), rheometry, Berkovich nanoindentation, and shear testing. Dynamic TGA measurements were performed under nitrogen at a heating rate of 10 °C min^{-1} using a TGA Q50 (TA Instruments, New Castle, Delaware, USA). Oscillatory temperature ramp experiments were conducted using a HAAKE MARS III Rheometer (Thermo Fisher Scientific, Karlsruhe, Germany) to measure the storage modulus (G'), loss modulus (G''), and loss tangent (tan δ, defined as G''/G') as a function of temperature. Disposable parallel plates (8 mm diameter) were used with a gap of 1 mm, a heating rate of 10 °C min^{-1}, a strain amplitude of 0.1%, and an angular frequency of 1 Hz. TGA and rheological measurements were repeated three times for each cured sample. The 5 wt% decomposition temperature ($T_{d,5\ wt\%}$) and glass transition temperature (T_g) were extracted from the corresponding curves and are reported as mean ± standard deviation. Representative curves are shown in Fig. 5A and B. Nanoindentation tests were performed using an iMicro Nanoindenter equipped with an InForce 1000 transducer and an optical microscope (KLA, Milpitas, California, USA). To minimize substrate effects, c-EIS and c-CE were prepared on slide glass with a thickness of ~200 μm. The Poisson ratio of both samples was assumed to be 0.3. All nanoindentations were conducted at a constant strain rate of 0.05 s^{-1} up to a maximum load of 200 mN. Simultaneously, continuous stiffness measurement (CSM) was applied at an oscillatory frequency of 110 Hz to measure the elastic modulus and hardness as functions of nanoindentation depth. After the nanoindentation tests, residual impressions were subsequently observed by the optical microscopy. To ensure statistical reliability, nanoindentation was performed at nine different locations on each sample. Shear tests were carried out using a DAGE 4000 equipped with a DS200 Cartridge (Nordson, Westlake, Ohio, USA) at a shear speed of 80 μm s^{-1}, a shear height of 40 μm, and a minimum shear force threshold of 2 kgf. The specimens were prepared by bonding a silicon chip (2.0 × 2.0 × 0.4 mm^3) onto a Cu substrate using r-CE and r-EIS, followed by curing under the conditions described above. Seven shear tests were conducted for each material and condition, and the results are reported as mean ± standard deviation. Accelerated humid-aging tests were conducted to evaluate the service reliability of the adhesive joints under humid conditions. The c-EIS and c-CE die-attach specimens were placed in a sealed chamber containing a saturated NaCl aqueous solution and aged at 40 °C for 72 h. This condition provides an equilibrium relative humidity of approximately 75% RH based on the humidity fixed point of saturated NaCl solution [15]. After humid aging, the specimens were removed from the chamber and subjected to shear testing under the same conditions described above. For degradation studies in aqueous environments, c-EIS and c-CE were immersed in 50 wt% AcOH(aq), PBS, and 1 M NaOH(aq) at room temperature. Weight retention was monitored by measuring the sample mass before immersion and at one-day intervals thereafter. For c-EIS in 1 M NaOH(aq), the mass change was continuously monitored in real time for up to 90 min due to its rapid degradation behaviour. For FTIR analysis of the alkaline degradation product, c-EIS was immersed in 1 M NaOH(aq) at room temperature until no visible solid residue remained. The resulting degradation solution was collected and dried at 120 °C to obtain the degraded/recovered product, denoted as DR-c-EIS. The FTIR spectrum of DR-c-EIS was recorded using the same FTIR setup described above.

3. Results and Discussion

3.1. Synthesis and molecular structure of EIS

The EIS hybrid resin was designed to integrate isosorbide-derived biomass segments and cycloaliphatic epoxide functionalities within a siloxane (Si–O–Si) inorganic backbone at the molecular level, as illustrated in Fig. 1. Unless otherwise specified, EIS refers to the representative batch, EIS-B1, used for structural characterization and property evaluation. The synthetic strategy exploits the dual reactivity of ECTMS. The methoxy groups of ECTMS can be hydrolysed to form silanols, which subsequently condense with the hydroxyl groups of isosorbide or with other silanol species. In parallel, unhydrolysed methoxy groups can react with the hydroxyl groups of isosorbide or with silanols via alcoholysis. The cycloaliphatic epoxide moieties remain intact for subsequent cationic curing.

The molecular structure of the synthesized EIS was investigated by FTIR spectroscopy (Fig. 2A and B). In the high-wavenumber region (Fig. 2A), the characteristic methoxy C–H stretching band of ECTMS at 2839 cm^{-1} is markedly attenuated in the EIS spectrum. This indicates that the trimethoxysilyl groups were substantially consumed through both hydrolysis-condensation and direct alcoholysis pathways during synthesis [16]. Concurrently, the O–H stretching band of isosorbide centred at 3363 cm^{-1} is significantly reduced [16]. Weak and broad residual absorption observed at around 3400 cm^{-1} can be attributed to remaining silanol (Si–OH) groups as well as hydrogen-bonded hydroxyl species within the hybrid network [16]. In the low-wavenumber region (Fig. 2B), a strong and broadened absorption band spanning 1000–1200 cm^{-1} is evident. This band is primarily assigned to Si–O–Si stretching vibrations and confirms the formation of a siloxane network backbone [17]. Notably, this broad envelope also includes contributions from Si–O–C stretching vibrations, consistent with the formation of silyl ether linkages via both condensation and direct alcoholysis between ECTMS and the secondary hydroxyl groups of isosorbide [17]. The pronounced attenuation of the methoxy C–H band at 2839 cm^{-1} further supports extensive conversion of Si–OCH_3 groups, thereby minimizing the likelihood of significant residual methoxy contributions in this region [17]. Importantly, the characteristic cycloaliphatic epoxide band at 883 cm^{-1} remains clearly visible in the EIS spectrum. This demonstrates that the epoxide functionalities of ECTMS are preserved during the condensation process and remain available for subsequent cationic ring-opening polymerization [16].

The molecular weight distribution of the synthesized EIS was determined by triple-detection GPC (Fig. 2C). The representative batch, EIS-B1, exhibited an extremely broad molecular weight distribution spanning approximately 3 × 10^2 to 2 × 10^6 g mol^{-1} with M_n = 2,336 g mol^{-1} and M_w = 27,632 g mol^{-1}, corresponding to a polydispersity index (PDI) of 11.8 (Table S3). This broad distribution is characteristic of sol–gel condensation systems and can be attributed to competitive hydrolysis, alcoholysis, and multidirectional condensation involving the trifunctional trimethoxysilyl groups of ECTMS and the two hydroxyl groups of isosorbide, which generate a heterogeneous mixture of oligomeric and branched species [18]. To evaluate batch-to-batch reproducibility, three independently synthesized EIS batches, denoted as EIS-B1, EIS-B2, and EIS-B3, were analysed by GPC under the same

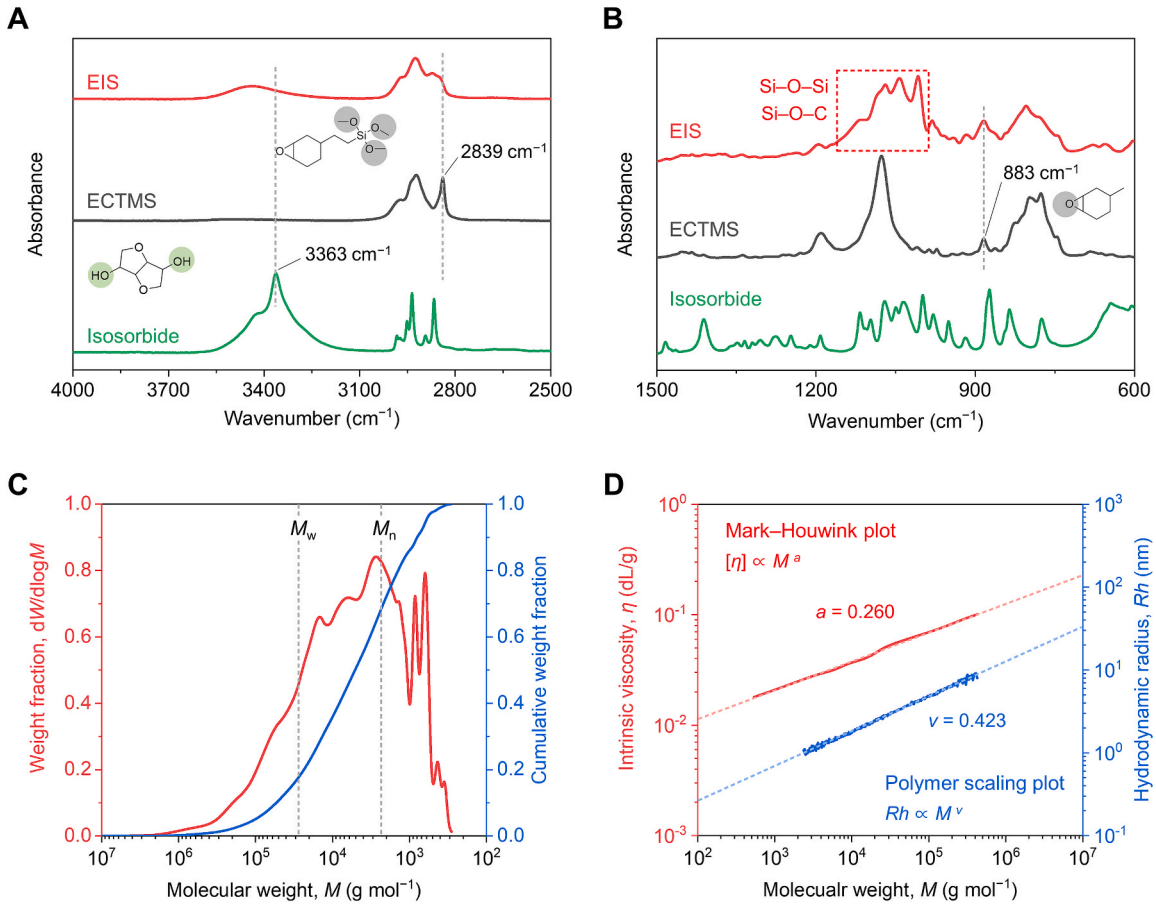

Fig. 2. Spectroscopic and chromatographic characterization of the synthesized EIS hybrid resin. (A) High- and (B) low-wavenumber FTIR spectra of isosorbide, ECTMS, and EIS. (C) Representative GPC traces and cumulative weight fraction of EIS, showing its broad molecular weight distribution. (D) Mark–Houwink plot (intrinsic viscosity vs molecular weight) and polymer scaling plot (hydrodynamic radius vs molecular weight) derived from triple-detection GPC analysis. Dashed lines represent the fitted curves.

conditions (Fig. S2 and Table S3). All three batches exhibited comparable broad molecular weight distributions, with average values of M_n = 2,168 ± 189 g mol^{-1}, M_w = 27,502 ± 424 g mol^{-1}, and PDI = 12.7 ± 1.0. The resin recoveries were also highly consistent, with an average recovery of 85.7 ± 0.4%. These results support the batch-to-batch reproducibility of the EIS synthesis under the specified reaction conditions. The molecular architecture of the representative EIS batch in solution was further evaluated using Mark–Houwink and hydrodynamic scaling analyses derived from triple-detection GPC (Fig. 2D). The Mark–Houwink exponent (a) was determined to be 0.260, while the hydrodynamic scaling exponent (v) was 0.423. For comparison, a linear polystyrene standard (PS240K) analysed under identical conditions exhibited an a of 0.678 and v of 0.559 (Fig. S1), consistent with an expanded coil conformation in solution [19,20]. The substantially reduced exponents observed for EIS indicate a compact, globular-like molecular conformation rather than an extended linear architecture [19–21]. No abnormal scattering behaviour was observed within the analysed molecular weight range and the log–log plots exhibited consistent linear scaling. This suggests that the measured hydrodynamic parameters primarily reflect the intrinsic molecular architecture rather than intermolecular aggregation [21]. This compact structure is mechanistically consistent with the multifunctional nature of the reactants. The three methoxy groups of ECTMS enable multidirectional condensation, while the two hydroxyl groups of isosorbide facilitate multiple silyl ether linkages. Collectively they promote branched oligomer growth. The *Rh* distribution (Fig. 2D), ranging from approximately 1 to 10 nm, further supports the presence of compact, branched species spanning a wide size distribution. The EIS resin therefore represents a statistical distribution of partially condensed oligomeric species rather than a single well-defined molecular structure, which is typical for alkoxysilane condensation systems.

The molecular structure of EIS was further elucidated by liquid-state ^{1}H, ^{13}C, and ^{29}Si NMR spectroscopy (Fig. 3A–C). The molecular motifs derived from these analyses are illustrated in Fig. 3D. In the ^{1}H NMR spectrum of EIS (Fig. 3A), the hydroxyl proton signals of isosorbide (g, g'), clearly observed in the neat spectrum, are absent in EIS. This suggests the hydroxyl groups are involved in silylation [22]. The attenuation of the methoxy proton resonance (p) of the trimethoxysilyl group in the ^{1}H NMR spectrum is accompanied by a significant reduction of the corresponding methoxy carbon signal (p) in the ^{13}C NMR spectrum (Fig. 3B), supporting substantial alkoxy conversion [18]. No distinct Si–OH proton resonance could be unambiguously assigned in the ^{1}H NMR spectrum, likely due to rapid proton exchange and severe signal broadening, as well as overlap with the isosorbide-derived resonances. These ^{1}H and ^{13}C NMR observations together strongly support that the hydroxyl groups of isosorbide reacted with the trimethoxysilyl functionalities of ECTMS. Despite this chemical transformation, the characteristic resonances corresponding to the bicyclic framework of isosorbide (a–f) remain clearly identifiable in both the ^{1}H and ^{13}C NMR spectra and confirm that the rigid bicyclic core structure is preserved. The bicyclic protons (a–f) exhibit noticeable broadening and slight chemical-shift changes relative to neat isosorbide, consistent with modification of the local electronic environment following silyl ether formation. The corresponding carbon resonances meanwhile show minimal chemical-shift variation in the ^{13}C spectrum, supporting retention of the isosorbide backbone [22]. Resonances associated with

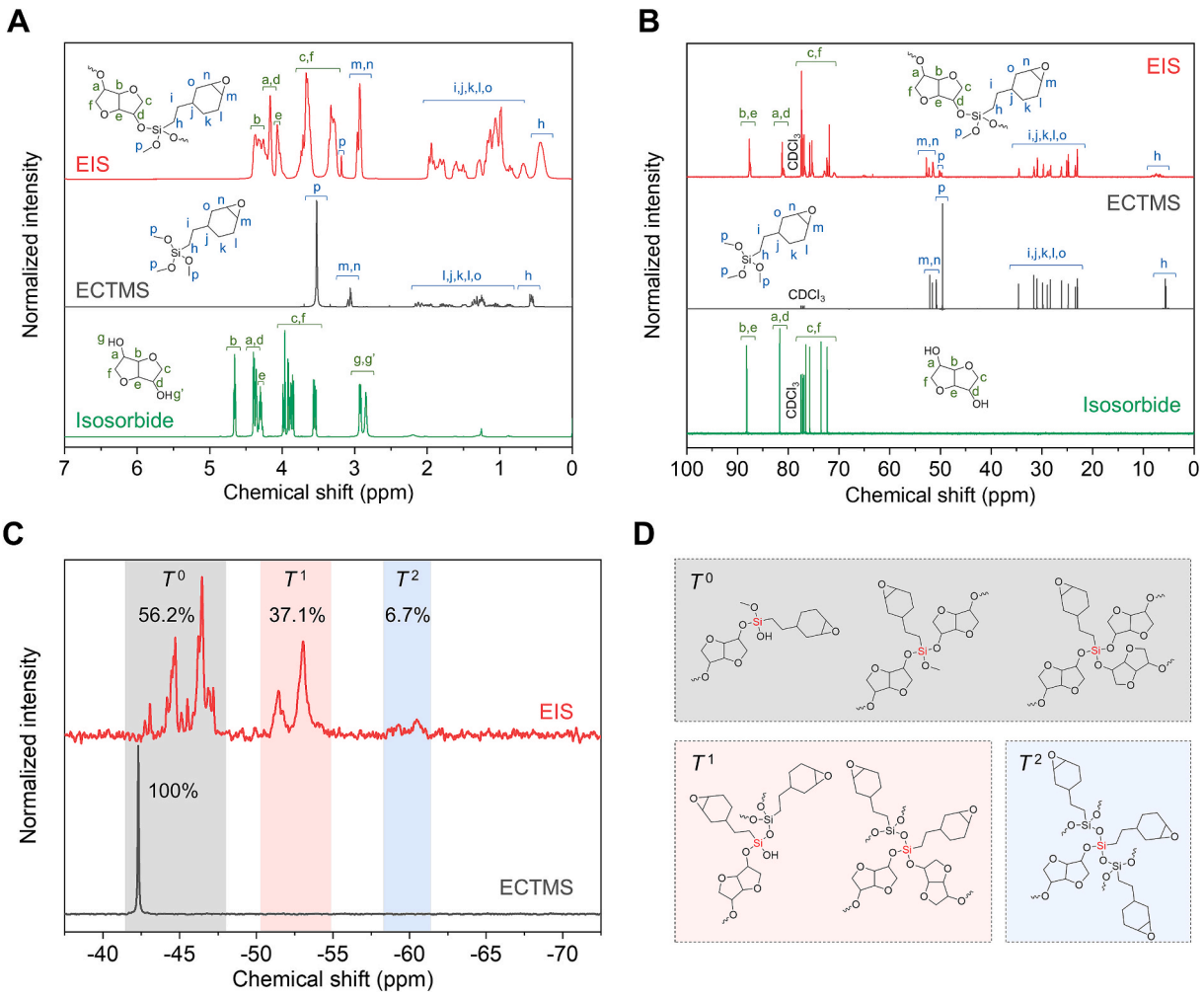

Fig. 3. NMR characterization of the synthesized EIS hybrid resin. (A-C) ^{1}H, ^{13}C, ^{29}Si NMR spectra of EIS; (D) Proposed molecular motifs corresponding to the observed T^0, T^1, and T^2 species.

the cycloaliphatic epoxide moiety (h–o) remain clearly detectable in both the ^{1}H and ^{13}C NMR spectra. In particular, the epoxide ring signals (m, n) are preserved in both spectra. This confirms that the epoxide functionality is retained during the condensation process [18]. The ^{29}Si NMR spectrum (Fig. 3C) provides direct insight into the silicon condensation state. Whereas neat ECTMS exhibits a single T^0 resonance corresponding to the trialkoxysilane environment, EIS displays a distribution of T^0 (56.2%), T^1 (37.1%) and T^2 (6.7%) species that demonstrates an intermediate condensation degree. The emergence of T^1 and T^2 species confirms the formation of Si–O–Si linkages [17]. Notably, the T^0 region in EIS is resolved into multiple components and is slightly shifted relative to the single T^0 resonance of neat ECTMS, which indicates the silicon chemical environment is modified upon reaction [17]. These features indicate that the T^0 species are not simply residual free ECTMS, but rather a distribution of low-condensed silicon environments bearing residual alkoxy, silanol, and/or isosorbide-derived silyl ether substituents. Based on the overall distribution of T^0, T^1 and T^2 species, Fig. 3D depicts representative molecular moieties corresponding to these silicon environments. In this model, T^0 units represent silicon centres bearing three non-siloxane substituents, T^1 units contain one Si–O–Si linkage, and T^2 units contain two Si–O–Si linkages. Collectively they form partially condensed siloxane oligomers that incorporate silylated isosorbide units while retaining pendent cycloaliphatic epoxide groups. These results are fully consistent with the FTIR and GPC analyses presented in Fig. 2.

3.2. Comparative study of curing kinetics

The molecular structures of EIS, CE, and TAG are shown in Fig. 4A. To enable a direct comparison of curing kinetics, r-EIS and r-CE were prepared as described in the Materials and Methods section. The thermal curing behaviour was first evaluated by dynamic DSC (Fig. 4B). The r-EIS formulation exhibits T_{peak} of 122.4 ± 2.1 °C and ΔH_{total} of 216.6 ± 0.5 J g^{-1}, both lower than those of r-CE (T_{peak} = 149.7 ± 3.8 °C and ΔH_{total} = 449.5 ± 3.3 J g^{-1}). In addition, the exothermic peak of r-EIS is sharper and confined within a narrower temperature range, whereas r-CE displays a broader curing profile. These features indicate that the curing reaction of r-EIS occurs over a narrower temperature range and proceeds more rapidly than that of r-CE. The smaller ΔH_{total} of r-EIS arises from the lower epoxide content per unit mass due to the incorporated siloxane and isosorbide segments. To quantitatively analyse the curing kinetics, isothermal DSC experiments were conducted at 110, 115, and 120 °C. Representative heat-flow curves at 120 °C are shown in Fig. 4C, while the corresponding data at 110 and 115 °C are provided in Figs. S3A and S3B, respectively. At all temperatures, both systems exhibit bell-shaped heat-flow profiles characteristic of autocatalytic curing reactions commonly observed in epoxy thermosets [23]. At 120 °C, r-EIS approaches completion within approximately 10 min, whereas r-CE requires nearly 100 min under identical conditions. These results demonstrate the markedly accelerated curing kinetics of r-EIS. The fractional conversion, $\alpha(t)$, was calculated according to .

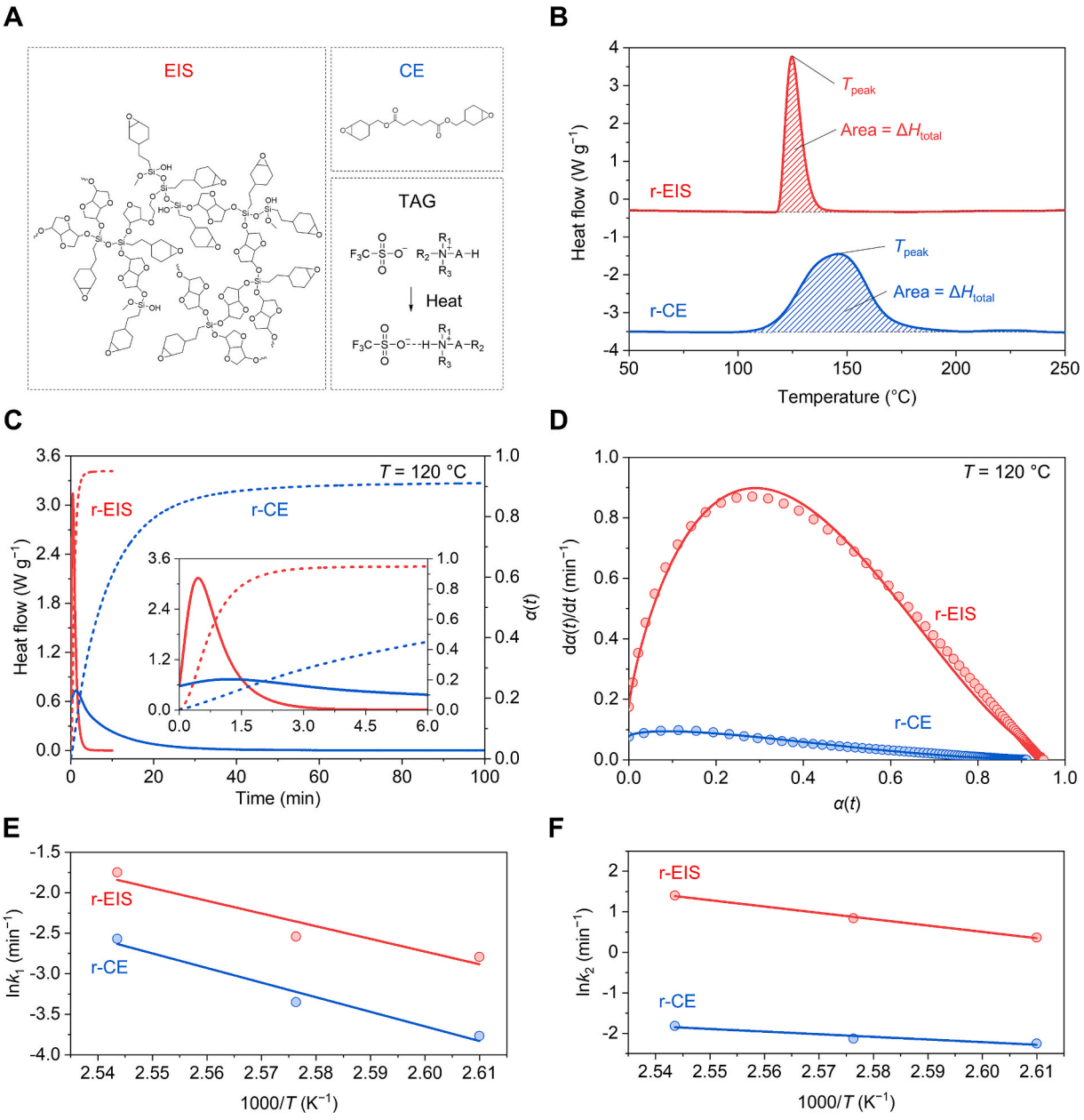

Fig. 4. Thermal curing behaviour of r–EIS (red) and r–CE (blue). (A) Molecular structures of EIS, CE, and TAG. (B) Representative dynamic DSC thermograms. (C) Representative isothermal DSC heat-flow curves at 120 °C (solid lines: heat flow; dashed lines: $\alpha(t)$). (D) Conversion-rate profiles at 120 °C fitted with the modified autocatalytic model (solid lines). (E, F) Arrhenius plots of the non-autocatalytic (k_1) and autocatalytic (k_2) rate constants.

$$\alpha(t) = \frac{H(t)}{\Delta H_{total}},$$

where $H(t)$ is the heat released up to time t during isothermal curing. The corresponding conversion-rate profiles at 120 °C are presented in Fig. 4D and confirm the substantially higher reaction rates of r-EIS across the entire conversion range. The isothermal kinetic data were fitted using the modified autocatalytic model,

$$\frac{d\alpha(t)}{dt} = (k_1 + k_2\alpha(t)^m)(1-\alpha(t))^n,$$

where k_1 and k_2 are the rate constants corresponding to the non-autocatalytic and autocatalytic contributions, respectively, and m and n are the associated reaction orders [24]. The fitted curves show excellent agreement with the experimental data at all three temperatures (Fig. 4D and Figs. S3C,D), and the extracted kinetic parameters are summarized in Table 1. Overall, both the k_1 and k_2 values for r-EIS are higher than those of r-CE, indicating that the curing reaction of r-EIS proceeds more rapidly throughout the entire conversion range. The temperature dependence of the rate constants was analysed using the Arrhenius relationship,

$$k_i = A_i \exp\left(-\frac{E_{ai}}{RT}\right) (i = 1, 2),$$

where A_1 and A_2 are the pre-exponential factors corresponding to k_1 and k_2, respectively, and E_{a1} and E_{a2} are the associated activation energies. The resulting Arrhenius parameters are also summarized in Table 1. As shown in Fig. 4E, F and Table 1, r-CE exhibited a pronounced decrease from E_{a1} to E_{a2}, reflecting the progressive transition from an initially non-autocatalytic pathway to a hydroxyl-assisted autocatalytic regime as curing proceeds. The high E_{a1} for the non-autocatalytic pathway arises from the energetically demanding direct protonation of the

Table 1
Kinetic and Arrhenius parameters for the curing of r-EIS and r-CE. Values are reported as mean ± standard deviation from three independent DSC kinetic analyses.

Material		r-EIS			r-CE		
Curing temperature (°C)		110	115	120	110	115	120
Kinetic parameters	k_1 (min^{-1})	0.066 ± 0.004	0.081 ± 0.004	0.174 ± 0.011	0.024 ± 0.002	0.038 ± 0.003	0.078 ± 0.002
	k_2 (min^{-1})	1.416 ± 0.083	2.223 ± 0.087	4.018 ± 0.055	0.107 ± 0.001	0.127 ± 0.008	0.171 ± 0.013
	m	0.736 ± 0.026	0.703 ± 0.036	0.835 ± 0.082	0.545 ± 0.050	0.540 ± 0.029	0.619 ± 0.017
	n	1.902 ± 0.202	1.741 ± 0.095	1.914 ± 0.110	2.307 ± 0.140	2.063 ± 0.121	2.060 ± 0.025
Arrhenius parameters	A_1 (min^{-1})	$(3.4 \pm 0.1) \times 10^{16}$			$(6.3 \pm 0.3) \times 10^{18}$		
	E_{a1} (kJ mol^{-1})	134.1 ± 3.8			151.5 ± 3.7		
	A_2 (min^{-1})	$(8.0 \pm 0.5) \times 10^{17}$			$(2.4 \pm 0.1) \times 10^{6}$		
	E_{a2} (kJ mol^{-1})	131.7 ± 6.4			57.1 ± 4.0		

epoxide ring by the Brønsted acid generated from TAG in the absence of hydrogen-bond donors. In contrast, the lower E_{a2} reflects the involvement of hydroxyl groups formed during epoxide ring opening, which can facilitate oxonium ion formation through proton-transfer-assisted epoxide activation [25].

In contrast, r-EIS exhibited comparable E_{a1} and E_{a2} values within experimental error (Table 1). This indicates that the apparent activation barrier remains similar during the early and later stages of curing, unlike the reference r-CE system. Therefore, the curing behaviour of r-EIS is described as pseudo-autocatalytic-like, reflecting the comparable apparent activation barriers in the early and later curing stages. The higher k_1 value and lower early-stage activation barrier of r-EIS compared with r-CE suggest that initial epoxide activation is more favourable in the r-EIS formulation, leading to rapid curing from the early stage of polymerization. Considering the silanol-containing silicon–oxygen environments identified in EIS, this accelerated curing behaviour may be associated with hydroxy/silanol-assisted cationic epoxide activation. However, the similarity between E_{a1} and E_{a2} does not, by itself, uniquely prove a specific silanol-mediated mechanism. Previous studies have reported that hydroxy- or silanol-containing species can influence cationic epoxy curing through activated-monomer-type pathways or proton-donor cocatalytic effects. Crivello and Liu reported that epoxy alcohol monomers undergo rapid cationic photopolymerization and that hydroxy groups enhance epoxide ring-opening polymerization through an activated monomer mechanism [26]. Atif et al. reported that silanol-rich carbon black surfaces substantially reduce the activation energy of cationic epoxy curing [27]. Cho et al. reported that silica nanoparticles bearing surface silanol groups can enhance the curing rate of SU-8 epoxy photoresists by acting as proton-donor cocatalysts [28]. In addition, Chen et al. reported that silane-containing alicyclic epoxy systems exhibit modified cationic thermopolymerization kinetics depending on the silane environment [29]. These literature precedents support the possibility that silanol-containing silicon–oxygen environments in EIS can facilitate cationic epoxy curing and contribute to the accelerated early-stage curing behaviour of r-EIS. As discussed in Section 3.1, the T^0 species observed in the ^{29}Si NMR spectrum are not simply assigned to residual free ECTMS, but to low-condensed silicon environments bearing residual alkoxy, silanol, and/or Si–O–C(isosorbide) substituents. Therefore, the pseudo-autocatalytic-like curing behaviour of r-EIS is interpreted as being consistent with the possible contribution of silanol-containing silicon–oxygen environments to the accelerated cationic curing process.

Overall, these kinetic features indicate that r-EIS undergoes faster cationic curing than the reference r-CE formulation. This behaviour is consistent with the combined effects of favourable early-stage epoxide activation, silanol-containing silicon–oxygen environments, and the heterogeneous oligomeric structure of EIS. This fast-curing behaviour may offer potential advantages for energy-efficient processing and shortened production cycles.

3.3. Comparative study of thermo-mechanical properties and degradation behaviour

To evaluate the thermal properties, thermomechanical properties, thermal stability, and mechanical performance of the cured networks, r-EIS and r-CE were cured to yield c-EIS and c-CE, respectively, as described in the Materials and Methods section. TGA, temperature-dependent oscillatory rheology, and Berkovich nanoindentation were then performed, and the results are summarized in Fig. 5A–F. The thermal stability of the cured samples was examined by dynamic TGA (Fig. 5A). The $T_{d,5\ wt\%}$ was 284.6 ± 2.2 °C for c-EIS and 263.5 ± 1.8 °C for c-CE. Within the measured temperature range (up to 350 °C), c-EIS retained a higher residual mass than c-CE, and the derivative thermogravimetric (DTG) curves indicated that the primary decomposition event occurred at higher temperature. The improved thermal stability of c-EIS is attributed to the thermally robust siloxane backbone together with the rigid bicyclic structure of isosorbide, which collectively enhance network stability at elevated temperatures [13,17].

The viscoelastic properties were characterized by dynamic oscillatory rheology (Fig. 5B). Both materials exhibited a glassy region followed by a decrease in G' associated with the glass-to-rubber transition. T_g, defined as the peak of tan δ, was 109.2 ± 1.6 °C for c-EIS and 88.2 ± 0.7 °C for c-CE [30]. In addition, c-EIS maintained a higher modulus in the rubbery plateau region owing to an increased effective network density compared with c-CE, resulting in a smaller modulus reduction across T_g. This behaviour suggests that the rigid bicyclic structure of isosorbide increases segmental constraint within the network, while the covalently integrated siloxane framework enhances the thermal stability of the backbone. The cooperative effect of these two structural motifs leads to a higher glass transition temperature and improved modulus retention at elevated temperatures. Furthermore, at higher temperatures, c-CE exhibited a pronounced decrease of its modulus associated with the onset of thermal degradation. In contrast, c-EIS retained its modulus over a broader temperature range without degradation-induced softening. This thermomechanical behaviour is consistent with the TGA results (Fig. 5A), which show delayed decomposition and higher thermal resistance for c-EIS relative to c-CE. Together, the TGA/DTG and rheological results demonstrate that c-EIS exhibits improved thermal stability and thermomechanical performance compared with c-CE, including higher decomposition resistance, higher T_g, and better modulus retention at elevated temperature.

Room-temperature nanomechanical properties were evaluated using Berkovich nanoindentation (Fig. 5C–F). The load–depth curves (Fig. 5C) showed shallower penetration depth and steeper unloading slopes for c-EIS compared to c-CE under identical indentation conditions. The less pronounced residual impressions observed for c-EIS (Fig. 5D) indicated reduced plastic deformation. This was quantitatively reflected in the higher elastic recovery ratio of c-EIS (46.6 ± 0.6%) compared to c-CE (38.8 ± 0.5%), as shown in Fig. 5E. Such enhanced elastic recovery behaviour has been widely reported for epoxy–siloxane hybrid systems, where the incorporation of flexible siloxane segments improves elastic resilience while maintaining network integrity under mechanical loading [31–33]. CSM further revealed that c-EIS consistently exhibited

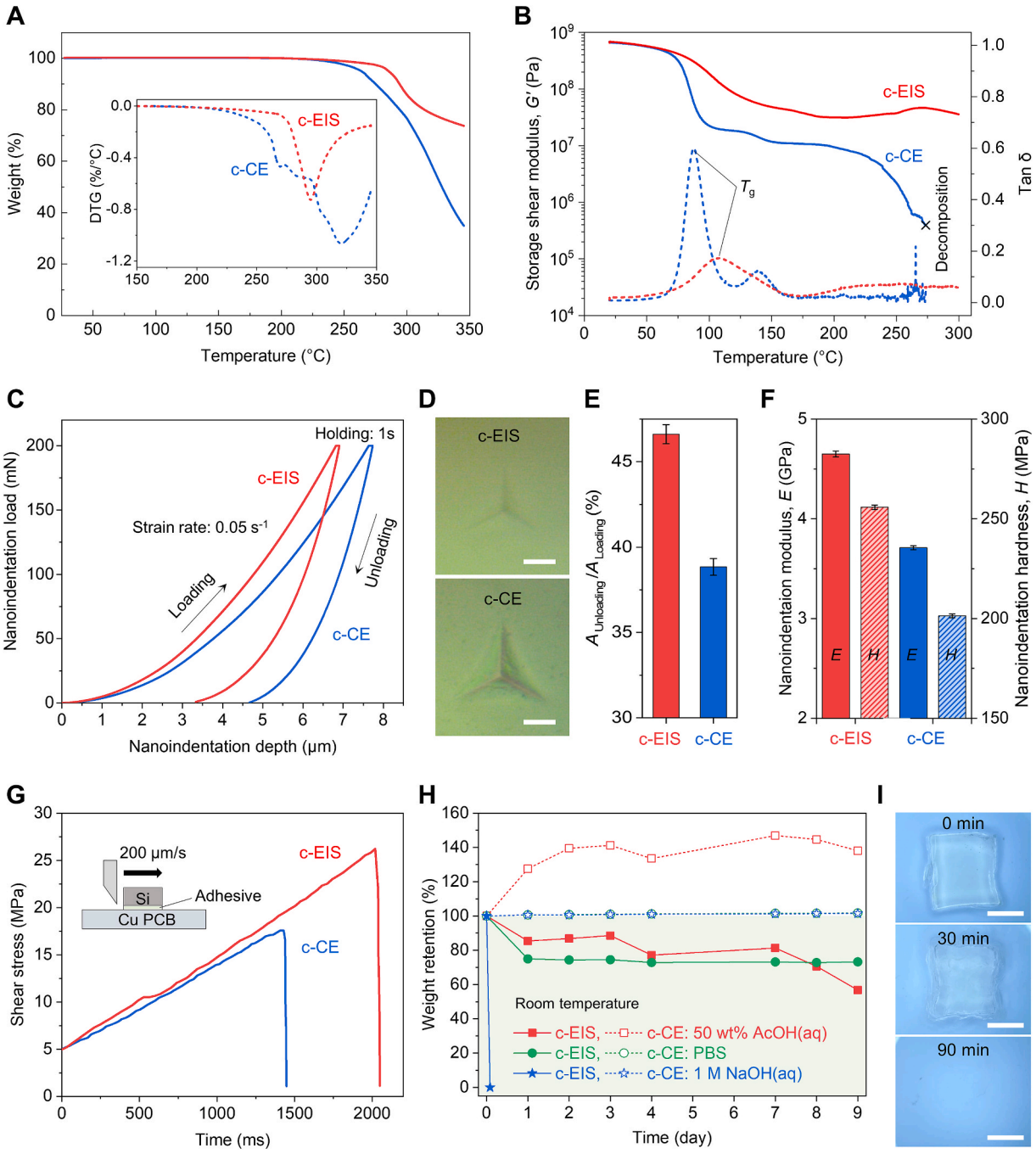

Fig. 5. Thermal, mechanical, adhesive, and degradation behaviours of c-EIS and c-CE. (A) Representative TGA curves with a DTG inset. (B) Representative temperature dependence of G′ and tan δ obtained from dynamic oscillatory rheology. (C-F) Nanoindentation results: representative load–depth curves, residual surface impressions after indentation (scale bar: 20 μm), elastic recovery ratio derived from the indentation loading–unloading curves, and elastic modulus and hardness extracted at an indentation depth of 5 μm. (G) Representative shear strength measured in a die-attach configuration (Si chip/adhesive/Cu substrate). (H) Weight retention of c-EIS and c-CE after immersion in 50 wt% AcOH(aq), PBS, and 1 M NaOH(aq) at room temperature. Solid symbols represent c-EIS and open symbols represent c-CE. (I) Photographs showing the degradation of c-EIS in 1 M NaOH(aq) at room temperature after 0, 30, and 90 min. (scale bar: 1 cm).

higher elastic modulus and hardness over the measured indentation depth range (Fig. S4). The average values extracted at an indentation depth of 5 μm (Fig. 5F) confirmed that both the modulus (4.65 ± 0.03 GPa) and hardness (255.8 ± 1.1 MPa) of c-EIS exceeded those of c-CE (3.71 ± 0.02 GPa and 201.4 ± 1.0 MPa), indicating improved resistance to both elastic and plastic deformation [31].

The adhesive performance was evaluated in a die-attach configuration using a silicon chip bonded to a copper substrate (Fig. 5G). The maximum shear strength reached 27.5 ± 2.3 MPa for c-EIS, compared to 17.6 ± 1.9 MPa for c-CE. Since both systems contain hydroxyl groups generated during the cationic polymerization, the enhanced adhesion of c-EIS is attributed to additional siloxane-mediated interactions with oxide surfaces. This is consistent with previous reports that siloxane-containing networks are known to interact strongly with oxide surfaces through hydrogen bonding and silanol–surface interactions [34,35]. To further evaluate service reliability under humid conditions, accelerated humid-aging tests were performed on c-EIS and c-CE die-attach specimens at 40 °C and 75% RH for 72 h using a saturated NaCl aqueous solution (Fig. S5). After humid aging, c-EIS and c-CE exhibited shear strengths of 26.9 ± 2.9 MPa and 17.0 ± 2.5 MPa,

respectively, which were comparable to their initial values. These results indicate that both adhesive joints maintained their mechanical integrity after the aging test. The retained high shear strength of c-EIS suggests that the adhesive joint remains stable under the tested moderate humid-aging condition.

To evaluate the aqueous durability and degradation behaviour of the cured networks, the samples were immersed in 50 wt% AcOH(aq), PBS, and 1 M NaOH(aq) at room temperature (Fig. 5H and I). While the reference epoxy (c-CE) exhibited slight mass gain in neutral and basic media and more pronounced swelling in the acidic solution, c-EIS showed a clear pH-dependent mass loss behaviour. Under acidic and neutral conditions, c-EIS exhibited gradual and moderate mass loss over the observation period (Fig. 5H). This slow degradation is attributed to the partial hydrolysis of Si–O–C silyl ether linkages. Although hydrolysis can occur through nucleophilic attack by water, the reaction proceeds slowly at near-neutral pH due to the weak nucleophilicity of water and the relatively stable Si—O—C bond [36,37]. Under acidic conditions, protonation of the bridging oxygen in the Si–O–C linkage increases the electrophilicity of the silicon centre and this facilitates nucleophilic attack by water through an acid-catalysed pathway. Nevertheless, the overall degradation rate remains limited because water is a relatively weak nucleophile, resulting in slow hydrolysis and limited chain scission [36,37]. In contrast, under alkaline conditions, hydroxide ions act as strong nucleophiles that directly attack the silicon centre via a bimolecular substitution mechanism (S_N2-Si). They then efficiently cleave Si—O—C bonds and rapidly disintegrate the network. As a result, c-EIS undergoes near-complete macroscopic degradation within approximately 90 min in 1 M NaOH(aq) at room temperature, leaving no visible bulk solid residue (Fig. 5I). To provide spectroscopic evidence for the chemical changes associated with alkaline degradation, FTIR spectra of c-EIS and the degraded/recovered product were compared (Fig. S6). The dried residue recovered from the 1 M NaOH(aq) degradation solution after alkaline degradation of c-EIS is denoted as DR-c-EIS. The FTIR spectrum of DR-c-EIS differs markedly from that of the original c-EIS network. The most pronounced spectral changes are observed in the 1000–1200 cm^{-1} broad envelope associated with Si–O–Si stretching vibrations and overlapping Si–O–C stretching contributions. These changes indicate alteration of the silicon–oxygen bonding environment after alkaline degradation, consistent with cleavage of alkali-labile Si–O–C silyl ether linkages and disruption of the crosslinked epoxy–silane network. DR-c-EIS also exhibits a broad absorption over the 2500–3700 cm^{-1} region, which is assigned to hydrogen-bonded O–H stretching vibrations from hydroxyl- or silanol-containing degradation products, adsorbed water, and hydrated sodium-containing residues. The broadening of this region, together with the less-defined aliphatic C–H stretching bands at 2950–2850 cm^{-1}, further indicates a substantial change in the chemical composition and hydrogen-bonding environment of the recovered degradation product. The intense bands observed at 1426 and 877 cm^{-1} in DR-c-EIS may include contributions from carbonate or sodium-containing residues formed from residual NaOH during drying; NaOH can absorb atmospheric CO_2 to form sodium carbonate, and carbonate species show characteristic FTIR bands near 1460 and 880 cm^{-1} [38,39]. Therefore, these bands were not assigned directly to Si—O—C bond cleavage. Instead, the degradation mechanism was supported by the near-complete macroscopic degradation/mass loss of c-EIS in 1 M NaOH(aq) and the pronounced FTIR spectral changes in the Si–O–Si/Si–O–C stretching region.

Importantly, the degradation observed under acidic and neutral conditions proceeded more slowly and gradually over the multi-day immersion period compared with the rapid alkaline degradation. Together with the humid-aging shear test results, this behaviour suggests that c-EIS can maintain adhesive integrity over the tested aging period under the moderate humid-aging condition of 40 °C and 75% RH, while still undergoing slow hydrolytic degradation under non-alkaline aqueous environments. The pronounced degradation under alkaline conditions supports the role of Si–O–C silyl ether linkages as alkali-labile cleavage sites, enabling chemically triggered end-of-life degradation with a markedly faster response under basic conditions. In contrast, the c-CE exhibited significantly greater resistance to hydrolytic degradation under all tested conditions, which reflects the inherent chemical stability of its carbon-based network structure. The incorporation of hydrolytically labile silyl ether linkages in c-EIS therefore introduces a chemically addressable degradation pathway absent in the reference c-CE system. To place these results in a broader context, representative cycloaliphatic epoxy systems and literature-reported isosorbide-based epoxy thermosets are summarized in Table S4. Because resin structures, curing chemistries, catalyst systems, specimen geometries, and test methods differ substantially among these systems, direct quantitative comparison should be made cautiously. Nevertheless, this comparison helps clarify the distinctive combination of properties targeted in this work: molecular hybrid reinforcement, improved die-attach adhesion, retention of adhesion after humid aging, and alkaline-triggered degradation in a single EIS-based formulation.

Collectively, the results obtained for c-EIS show a higher $T_{d,5\ wt\%}$, higher T_g and rubbery plateau modulus, enhanced nanomechanical properties, higher adhesive shear strength, and chemically addressable degradation behaviour compared with the reference cycloaliphatic epoxy c-CE. These improvements are attributed to the molecular-level integration of rigid isosorbide segments with a covalently incorporated siloxane network and provide reinforcement without the use of extrinsic inorganic fillers. In addition, the incorporation of alkali-labile Si–O–C linkages introduces an alkaline-triggered degradation pathway, providing a potential strategy for end-of-life disassembly of thermoset adhesive materials.

4. Conclusion

In this study, we developed an epoxy-functionalized isosorbide–siloxane molecular hybrid resin, EIS, through the co-condensation of bio-derived isosorbide and an epoxy-functional alkoxysilane. The key innovation of this design is the molecular-level integration of rigid renewable isosorbide segments, an inorganic siloxane framework, cycloaliphatic epoxide groups, and hydrolytically labile silyl ether linkages within a single curable oligomer. This architecture enables filler-free reinforcement while preserving reactive epoxide functionalities for subsequent cationic curing. The EIS-based resin exhibited rapid cationic curing, while the resulting c-EIS network provided improved thermal stability, thermomechanical performance, nanomechanical properties, and die-attach adhesion compared with the reference cycloaliphatic epoxy system. In addition, the incorporation of Si–O–C silyl ether linkages provided a chemically addressable degradation pathway, enabling rapid alkaline degradation while maintaining stability under the tested ambient and moderate humid-aging conditions.

These results demonstrate that bio-derived organic segments and inorganic siloxane structures can be covalently integrated at the molecular level to achieve fast processing, high performance, and controlled end-of-life degradability in a single epoxy adhesive platform. From a practical perspective, the alkaline-triggered degradation of c-EIS could be useful for electronic device disassembly, debonding of adhesive joints, and recovery or recycling of bonded components and substrates at end-of-life. This molecular hybrid strategy offers a practical design framework for sustainable thermoset adhesives that require both service reliability and chemically triggered disassembly after use.

CRediT authorship contribution statement

Gwang-Mun Choi: Writing – review & editing, Writing – original draft, Visualization, Supervision, Project administration, Methodology, Investigation, Funding acquisition, Formal analysis, Data curation, Conceptualization. **Jin-Hyuk Oh:** Investigation. **Ki-Seok Jang:** Investigation. **Yong-Sung Eom:** Resources, Funding acquisition. **Kwang-**

Seong Choi: Resources, Funding acquisition.

Declaration of competing interest

The authors declare the following financial interests/personal relationships which may be considered as potential competing interests: The authors are inventors on a patent titled "Silyl ether isohexide-based organic–inorganic compound, method for preparing the same, and curable composition comprising the same," assigned to ETRI.

Acknowledgements

This work was supported by ETRI grants funded by the Korean government (25YB2500, 26YB1100, and 26CB1100) and by a Korea Evaluation Institute of Industrial Technology (KEIT) grant funded by the Ministry of Trade, Industry and Energy (RS-2025-02308294). The authors acknowledge the Korea Basic Science Institute (KBSI) for NMR measurements, the Wearable Platform Materials Technology Centre for nanoindentation experiments, and the Chungbuk Technopark (CBTP) for shear testing.

Appendix A. Supplementary data

Supplementary data to this article can be found online at https://doi.org/10.1016/j.eurpolymj.2026.114877.

Data availability

Data will be made available on request.

References

[1] J.C. Capricho, B. Fox, N. Hameed, Multifunctionality in epoxy resins, Polym. Rev. 60 (2020) 1–41, https://doi.org/10.1080/15583724.2019.1650063.
[2] A. Shundo, S. Yamamoto, K. Tanaka, Network formation and physical properties of epoxy resins for future practical applications, JACS Au 2 (2022) 1522–1542, https://doi.org/10.1021/jacsau.2c00120.
[3] M. Sangermano, N. Razza, J.V. Crivello, Cationic UV-curing: technology and applications, Macromol. Mater. Eng. 299 (2014) 775–793, https://doi.org/10.1002/mame.201300349.
[4] M. Sangermano, I. Roppolo, A. Chiappone, New horizons in cationic photopolymerization, Polymers 10 (2018) 136, https://doi.org/10.3390/polym10020136.
[5] X.-W. Jia, W.-L. Mu, Z.-B. Shao, Y.-J. Xu, Flame-retardant cycloaliphatic epoxy systems with high dielectric performance for electronic packaging materials, Int. J. Mol. Sci. 24 (2023) 2301, https://doi.org/10.3390/ijms24032301.
[6] Y. Zhou, N. Tran, Y.-C. Lin, Y. He, F.G. Shi, One-component, low-temperature, and fast cure epoxy encapsulant with high refractive index for LED applications, IEEE Trans. Adv. Packag. 31 (2008) 484–489, https://doi.org/10.1109/TADVP.2008.924233.
[7] H. Zou, S. Wu, J. Shen, Polymer/silica nanocomposites: preparation, characterization, properties, and applications, Chem. Rev. 108 (2008) 3893–3957, https://doi.org/10.1021/cr068035q.
[8] Y. Li, T.M. Krentz, L. Wang, B.C. Benicewicz, L.S. Schadler, Ligand engineering of polymer nanocomposites: from the simple to the complex, ACS Appl. Mater. Interfaces 6 (2014) 6005–6021, https://doi.org/10.1021/am405332a.
[9] J.M. Sadler, A.-P.-T. Nguyen, F.R. Toulan, J.P. Szabo, G.R. Palmese, C. Scheck, S. Lutgen, J.J. La Scala, Isosorbide-methacrylate as a bio-based low viscosity resin for high performance thermosetting applications, J. Mater. Chem. A 1 (2013) 12579–12586, https://doi.org/10.1039/C3TA12918G.
[10] C.-H. Lee, H. Takagi, H. Okamoto, M. Kato, Improving the mechanical properties of isosorbide copolycarbonates by varying the ratio of comonomers, J. Appl. Polym. Sci. 127 (2013) 530–534, https://doi.org/10.1002/APP.37838.
[11] D. Yu, J. Zhao, W. Wang, J. Qi, Y. Hu, Mono-acrylated isosorbide as a bio-based monomer for the improvement of thermal and mechanical properties of poly (methyl methacrylate), RSC Adv. 9 (2019) 35532–35538, https://doi.org/10.1039/C9RA07548H.
[12] J. Hong, D. Radojčić, M. Ionescu, Z.S. Petrović, E. Eastwood, Advanced materials from corn: isosorbide-based epoxy resins, Polym. Chem. 5 (2014) 5360–5368, https://doi.org/10.1039/C4PY00514G.
[13] F. Fenouillot, A. Rousseau, G. Colomines, R. Saint-Loup, J.-P. Pascault, Polymers from renewable 1,4:3,6-dianhydrohexitols, isosorbide, isomannide and isoidide: a review, Prog. Polym. Sci. 35 (2010) 578–622, https://doi.org/10.1016/j.progpolymsci.2009.10.001.
[14] X.-H. Li, X. Zou, X. Zhang, X. Yin, X. Sui, Epoxy value measurement of E44 epoxy resin by various chemical titration method, ChemistrySelect 9 (2024) e202402677, https://doi.org/10.1002/slct.202402677.
[15] L. Greenspan, Humidity fixed points of binary saturated aqueous solutions, J. Res. Natl. Bur. Stand. A Phys. Chem. 81A (1977) 89–96, https://doi.org/10.6028/jres.081A.011.
[16] B. Stuart, Infrared Spectroscopy: Fundamentals and applications, Wiley, Chichester, 2004.
[17] C.J. Brinker, G.W. Scherer, Sol-Gel Science: the Physics and Chemistry of Sol-Gel Processing, Academic Press, Boston, 1990.
[18] F.D. Osterholtz, E.R. Pohl, Kinetics of the hydrolysis and condensation of organofunctional alkoxysilanes: a review, J. Adhes. Sci. Technol. 6 (1992) 127–149, https://doi.org/10.1163/156856192X00106.
[19] P.J. Flory, Principles of Polymer Chemistry, Cornell University Press, Ithaca, 1953.
[20] M. Rubinstein, R.H. Colby, Polymer Physics, Oxford University Press, New York, 2003.
[21] A.M. Striegel, W.W. Yau, J.J. Kirkland, D.D. Bly, Modern Size-Exclusion Liquid Chromatography, second ed., Wiley, Hoboken, 2009.
[22] L. Pezzana, A. Emanuele, R. Sesana, C. Delprete, E. Malmström, M. Johansson, M. Sangermano, Cationic UV-curing of isosorbide-based epoxy coating reinforced with macadamia nut shell powder, Prog. Org. Coat. 185 (2023) 107949, https://doi.org/10.1016/j.porgcoat.2023.107949.
[23] S. Vyazovkin, A.K. Burnham, J.M. Criado, L.A. Pérez-Maqueda, C. Popescu, N. Sbirrazzuoli, ICTAC Kinetics Committee recommendations for performing kinetic computations on thermal analysis data, Thermochim Acta 520 (2011) 1–19, https://doi.org/10.1016/j.tca.2011.03.034.
[24] S. Sourour, M.R. Kamal, Differential scanning calorimetry of epoxy cure: isothermal cure kinetics, Thermochim Acta 14 (1976) 41–59, https://doi.org/10.1016/0040-6031(76)80056-1.
[25] K. Horie, H. Hiura, M. Sawada, I. Mita, H. Kambe, Calorimetric investigation of polymerization reactions. III. Curing reaction of epoxides with amines, J. Polym. Sci. Part A-1, Polym. Chem. 8 (1970) 1357–1372, https://doi.org/10.1002/pol.1970.150080605.
[26] J.V. Crivello, S. Liu, Photoinitiated cationic polymerization of epoxy alcohol monomers, J. Polym. Sci., Part A: Polym. Chem. 38 (2000) 389–401, https://doi.org/10.1002/(SICI)1099-0518(20000201)38:3<389::AID-POLA1>3.0.CO;2-G.
[27] M. Atif, M.A. Hussain, F. Inam, R. Bongiovanni, Controlled cationic curing of epoxy composites with photochemically modified silanol encapsulated carbon black, J. Appl. Polym. Sci. 139 (2022) 52241, https://doi.org/10.1002/app.52241.
[28] J.-D. Cho, H.-T. Ju, Y.-S. Park, J.-W. Hong, Kinetics of cationic photopolymerizations of UV-curable epoxy-based SU8-negative photoresists with and without silica nanoparticles, Macromol. Mater. Eng. 291 (2006) 1155–1163, https://doi.org/10.1002/mame.200600124.
[29] J. Chen, B. Li, S. Zhang, H. Li, Effect of the presence of a silane coupling agent on reaction kinetics of cationic thermopolymerization of epoxy resin adhesive, Coatings 13 (2023) 1782, https://doi.org/10.3390/coatings13101782.
[30] K.P. Menard, Dynamic Mechanical Analysis: a Practical Introduction, CRC Press, Boca Raton, 2008.
[31] G.-M. Choi, J. Jin, D. Shin, Y.H. Kim, J.-H. Ko, H.-G. Im, J. Jang, D. Jang, B.-S. Bae, Flexible hard coating: glass-like wear resistant, yet plastic-like compliant, transparent protective coating for foldable displays, Adv. Mater. 29 (2017) 1700205, https://doi.org/10.1002/adma.201700205.
[32] G. Bae, G. Choi, C. Ahn, S. Kim, W. Kim, Y. Choi, D. Park, D. Jang, J. Hong, S. M. Han, B. Bae, S. Jeon, Flexible protective film: ultrahard, yet flexible hybrid nanocomposite reinforced by 3D inorganic nanoshell structures, Adv. Funct. Mater. 31 (2021) 2010254, https://doi.org/10.1002/adfm.202010254.
[33] H.-W. Yun, G.-M. Choi, H.K. Woo, S.J. Oh, S.-H. Hong, Superhydrophobic, antireflective, flexible hard coatings with mechanically ultra-resilient moth-eye structure for foldable displays, Curr. Appl Phys. 20 (2020) 1163–1170, https://doi.org/10.1016/j.cap.2020.07.001.
[34] T. Semoto, Y. Tsuji, K. Yoshizawa, Molecular understanding of the adhesive force between a metal oxide surface and an epoxy resin, J. Phys. Chem. C 115 (2011) 11701–11708, https://doi.org/10.1021/jp202785b.
[35] Y.-I. Lee, Y.-H. Choa, Adhesion enhancement of ink-jet printed conductive copper patterns on a flexible substrate, J. Mater. Chem. 22 (2012) 12517–12522, https://doi.org/10.1039/C2JM31381B.
[36] Y. Nishimura, J. Chung, H. Muradyan, Z. Guan, Silyl ether as a robust and thermally stable dynamic covalent motif for malleable polymer design, J. Am. Chem. Soc. 139 (2017) 14881–14884, https://doi.org/10.1021/jacs.7b08826.
[37] M.C. Parrott, J.C. Luft, J.D. Byrne, J.H. Fain, M.E. Napier, J.M. DeSimone, Tunable bifunctional silyl ether cross-linkers for the design of acid-sensitive biomaterials, J. Am. Chem. Soc. 132 (2010) 17928–17932, https://doi.org/10.1021/ja108568g.
[38] M. Mahmoudkhani, D.W. Keith, Low-energy sodium hydroxide recovery for CO_2 capture from atmospheric air—Thermodynamic analysis, Int. J. Greenhouse Gas Control 3 (2009) 376–384, https://doi.org/10.1016/j.ijggc.2009.02.003.
[39] S. Veerasingam, R. Venkatachalapathy, Estimation of carbonate concentration and characterization of marine sediments by Fourier transform infrared spectroscopy, Infrared Phys. Technol. 66 (2014) 136–140, https://doi.org/10.1016/j.infrared.2014.06.005.